The Astrophysical Journal, 806:37 (7pp), 2015 June 10 doi:10.1088/0004-637X/806/1/37

VARIABLE HARD-X-RAY EMISSION FROM THE CANDIDATE ACCRETING BLACK HOLE IN DWARF GALAXY HENIZE 2–10

Thomas J. Whalen[1,2], Ryan C. Hickox[1], Amy E. Reines[3,8], Jenny E. Greene[4], Gregory R. Sivakoff[5], Kelsey E. Johnson[6], David M. Alexander[7], and Andy D. Goulding[4]
[1] Department of Physics and Astronomy, Dartmouth College, 6127 Wilder Laboratory, Hanover, NH 03755, USA; ryan.c.hickox@dartmouth.edu
[2] Harvard-Smithsonian Center for Astrophysics, 60 Garden Street, Cambridge, MA 02138, USA
[3] Department of Astronomy, University of Michigan, 1085 South University Avenue, Ann Arbor, MI 48109, USA
[4] Department of Astrophysical Sciences, Princeton University, Princeton, NJ 08544, USA
[5] Department of Physics, University of Alberta, Edmonton, Alberta T6G 2E1, Canada
[6] Astronomy Department, University of Virginia, Charlottesville, VA 22904, USA
[7] Department of Physics, Durham University, South Road, Durham, DH1 3LE, UK
Received 2014 May 8; accepted 2015 April 13; published 2015 June 5

ABSTRACT

We present an analysis of the X-ray spectrum and long-term variability of the nearby dwarf starburst galaxy Henize 2–10. Recent observations suggest that this galaxy hosts an actively accreting black hole (BH) with mass $\sim 10^6\,M_\odot$. The presence of an active galactic nucleus (AGN) in a low-mass starburst galaxy marks a new environment for AGNs, with implications for the processes by which "seed" BHs may form in the early universe. In this paper, we analyze four epochs of X-ray observations of Henize 2–10, to characterize the long-term behavior of its hard nuclear emission. We analyze observations with *Chandra* from 2001 and *XMM-Newton* from 2004 and 2011, as well as an earlier, less sensitive observation with *ASCA* from 1997. Based on a detailed analysis of the source and background, we find that the hard (2–10 keV) flux of the putative AGN has decreased by approximately an order of magnitude between the 2001 *Chandra* observation and exposures with *XMM-Newton* in 2004 and 2011. The observed variability confirms that the emission is due to a single source. It is unlikely that the variable flux is due to a supernova or ultraluminous X-ray source, based on the observed long-term behavior of the X-ray and radio emission, while the observed X-ray variability is consistent with the behavior of well-studied AGNs.

Key words: galaxies: active – galaxies: dwarf – galaxies: evolution – galaxies: individual (Henize 2–10) – X-rays: galaxies

1. INTRODUCTION

The nearby (~9 Mpc) dwarf starburst galaxy Henize 2–10, exhibits intense star formation (e.g., Allen et al. 1976), while in the center of the galaxy, an X-ray point source (Kobulnicky & Martin 2010) and relatively luminous radio point source (Kobulnicky & Johnson 1999; Johnson & Kobulnicky 2003) were found to be co-spatial, suggesting the existence of an accreting low-mass active galactic nucleus (AGN) with a black hole (BH) of mass $\sim 10^6\,M_\odot$ (Reines et al. 2011; Reines & Deller 2012). This represented the first possible detection of an AGN in a dwarf starburst galaxy. Even if a large fraction of dwarf galaxies host massive BHs, they are challenging to detect as AGNs because the AGN emission is faint and its signatures can be swamped by surrounding star formation (e.g., Reines et al. 2013); X-ray observations can be one of the most effective methods for identifying AGNs in dwarf galaxies (e.g., Reines et al. 2014; Lemons et al. 2015; Secrest et al. 2015). If the existence of an AGN in He 2–10 is confirmed, it would serve as one of the best possible analogs for BH and galaxy growth in the early history of the universe (e.g., Reines et al. 2011). Most bulge-dominated galaxies contain supermassive BHs, however, the process by which the orignal "seed" BHs formed remains poorly constrained (e.g., Johnson & Bromm 2007; Volonteri 2010).

Currently, the available observational evidence for the central compact sources in He 2–10 favors its interpretation as a supermassive BH. The majority of its radio emission originates from a region $<3 \times 1$ pc in size (Reines & Deller 2012) and is consistent with being spatially coincident with the *Chandra* hard-X-ray point source at the dynamical center of the galaxy (Reines et al. 2011). Assuming that the radio and X-ray emission are produced by a BH, a comparison with the BH fundamental plane (Merloni et al. 2003) suggests that the mass is $\sim 10^6\,M_\odot$ (Reines et al. 2011). Alternatively, the X-ray emission could in principle come from an ultraluminous X-ray source that is powered by a stellar-mass BH (Roberts 2007). However, this cannot account for the observed compact radio flux (e.g., Middleton et al. 2013; Wolter et al. 2014), although we note that previous radio and X-ray observations are not strictly simultaneous. We can most likely rule out supernova (SN) remnants as the cause of the X-ray emission; there are no massive star-forming clusters coincident with the compact radio emission, rendering this scenario somewhat implausible, but not impossible. To more robustly constrain the nature of the compact central source in He 2–10 and to better constrain its mass, it is important to understand how its X-ray luminosity varies with time. This is the goal of the present paper.

The original evidence for the AGN in He 2–10 came in part from analysis of the spectrally hard, resolved point source in the 2001 *Chandra* observations. Here, we analyze data taken from *Chandra* (2001), *XMM-Newton* (2004 and 2011), and *ASCA* (1997) to obtain spectra at each epoch and a resulting measure of the long-term variability of the hard nuclear source. The temporal baseline of the observations is sufficient to probe variability on timescales reasonable for an intermediate-mass

[8] Hubble Fellow.

Table 1
Observation Details

Instrument	Detector	Obs.ID	Date	Exposure in ks (clean)	Net Counts 0.5–2 keV (2–8 keV)
Chandra	ACIS-S	2075	2001 Mar 23	20.0 (19.7)	983 (174)
XMM-Newton	pn	0202650101	2004 May 27	42.0 (29.3)	3216 (234)
XMM-Newton	pn	0672800101	2011 May 11	26.9 (17.6)	1863 (92)
ASCA	SIS	65017000	1997 Nov 30	39.8 (22.4)	197 (52)

Note. The details of each of the observations used in this paper. Observed net counts after background subtraction are listed for the 0.5–2 and 2–8 keV bands (see Section 2 for details of source extraction and background analysis). Exposure times listed are for the total exposure and the net exposure after cleaning for flares. We focus our analysis on the more sensitive *Chandra* and *XMM* observations, but include the earlier *ASCA* observation as a check on the baseline flux level for the source.

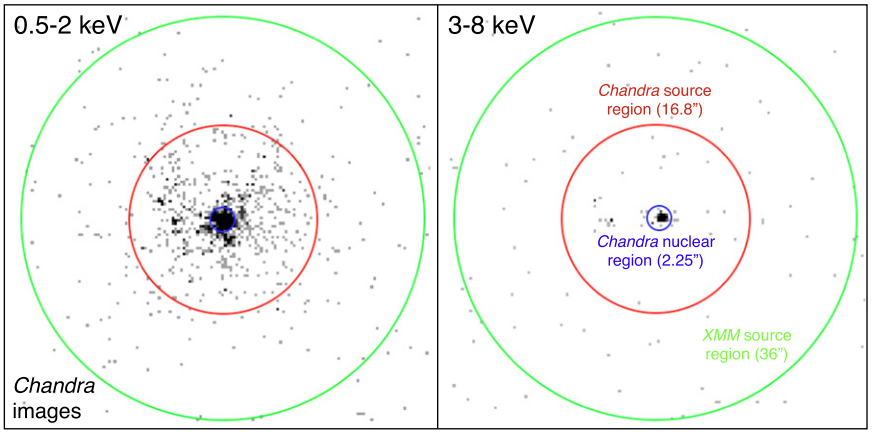

Figure 1. *Chandra* images in the soft (0.5–2 keV) and hard (3–8 keV) X-rays; energy ranges are chosen to clearly separate the soft diffuse component from the hard compact nuclear emission. The *XMM* source extraction region, as well as the two *Chandra* regions are superimposed. The excellent angular resolution of *Chandra* allows for clear imaging of the X-ray morphology. Widespread diffuse emission from star formation is seen in soft X-rays, while the central nuclear source is clearly seen at hard X-rays. *XMM-Newton* has significantly poorer angular resolution, thus a larger extraction region was required in order to include sufficient source flux.

BH or low-mass AGN, as shown by the small known sampling of these rare objects (Dewangan et al. 2008).

2. DATA REDUCTION AND SPECTRAL ANALYSIS

In this section we describe the spectral extraction process for each observation, with a focus on details of the sophisticated background modeling, which was required for the *XMM-Newton* and *ASCA* observations. All spectral analyses are performed using XSPEC v12.8.0 (Arnaud 1996). See Table 1 for the details of the observations. We will focus primarily on the more sensitive observations taken by *Chandra* in 2001 and *XMM* in 2004 and 2011, but will also include a discussion of the 1997 *ASCA* observation that provides a (less sensitive) baseline measurement of the source flux. Throughout the paper, uncertainties on X-ray measurements (fluxes, luminosities, and spectral parameters) represent 90% confidence intervals.

2.1. Chandra

The nuclear X-ray point source in He 2–10 was discovered in the 20 ks ACIS-S *Chandra* observation of He 2–10 on 2001 March 23 (Reines et al. 2011). The pipeline-reduced data from this observation (see Figure 1) were obtained from the HEASARC public archive and were reduced using the analysis tools of CIAO 4.5. Time filtering yielded 19.7 ks of cleaned exposure. For *Chandra* we defined two separate source extraction regions: a small region of radius 2.″25 at the nuclear region of the galaxy was used to measure the flux of the hard point source, and a larger region of radius 16.″8 was used to include the soft diffuse X-ray component. In either case, the background region was comprised of an annulus of outer radius 58 arcsec, excluding the larger (diffuse) source region and another point source about 45 arcsec away from the source. We note that the background level above 2 keV in the *Chandra* observation was much less prominent than in the *XMM* and *ASCA* observations. The spectrum, as well as the response and ancilliary files, were extracted using the `specextract` command. Due to the high signal-to-noise ratio (S/N) and low background, we used CIAO's built-in background subtraction rather than simultaneously fitting source and background spectra, as for the *XMM* and *ASCA* observations.

For all of the observations presented in this paper, the source spectrum is described with a model consisting of the power-law component to model the hard nuclear source and optically thin thermal (VMEKAL; Mewe et al. 1985; Liedahl et al. 1995) component to model the diffuse emission, with abundance values fixed to those obtained in Kobulnicky & Martin (2010) (0.78 for light elements and 0.29 for heavy elements), and allowing the normalization and temperature to float. We use a VMEKAL to match the spectral analysis of Reines et al. (2011), but note that fitting with an APEC model (Smith et al. 2001) has no significant effect on the results for the hard component. Following Kobulnicky & Martin (2010), we include Galactic absorption $N_{\rm H,Gal} = 5 \times 10^{20}\,{\rm cm}^{-2}$ on all

Table 2
Spectral Fitting Results

Observation	VMEKAL (Diffuse)		Power Law (Nuclear)				χ^2_ν (dof)
	kT (keV)	$F_{0.5-3\,\mathrm{keV}}$ (10^{-13} erg cm^{-2} s^{-1})	$N_{\mathrm{H,Nuclear}}$ (10^{22} cm^{-2})	Γ	$F_{2-10\,\mathrm{keV}}$ (10^{-13} erg cm^{-2} s^{-1})	$L_{2-10\,\mathrm{keV}}$[a] (10^{39} erg s^{-1})	
Chandra[b] (2001)	0.65 ± 0.03	2.06 ± 0.11	$4.61^{+1.67}_{-1.26}$	[1.8]	$3.28^{+0.73}_{-0.64}$	$3.18^{+0.71}_{-0.62}$	1.61 (46)
XMM[c] (2004)	$0.58^{+0.02}_{-0.03}$	$1.90^{+0.08}_{-0.05}$	<0.05	[1.8]	$0.68^{+0.08}_{-0.07}$	$0.66^{+0.08}_{-0.07}$	1.20 (661)
XMM[c] (2011)	$0.58^{+0.02}_{-0.03}$	$1.90^{+0.08}_{-0.05}$	<0.05	[1.8]	$0.44^{+0.09}_{-0.10}$	0.43 ± 0.09	1.20 (661)
ASCA (1997)	[0.65]	$2.89^{+0.89}_{-1.02}$	$0.30^{+3.83}_{-0.30}$	[1.8]	$1.79^{+1.66}_{-0.87}$	$1.73^{+1.61}_{-0.84}$	0.80 (70)

Notes. Best-fit spectral parameters obtained from modeling of the four X-ray spectra. The (unabsorbed) 2–10 keV fluxes were calculated based on the nuclear (power-law) component, while the (observed) 0.5–3 keV fluxes correspond to the diffuse (VMEKAL) component. Both components are modified by Galactic absorption with column density fixed at $N_{\mathrm{H,Gal}} = 9 \times 10^{20}$ cm^{-2}, and the VMEKAL component is absorbed by an additional component with column density fixed at $N_{\mathrm{H,Diffuse}} = 9.7 \times 10^{20}$ cm^{-2}. Parameters in the table that are fixed in the fits are identified with brackets. Uncertainties represent 90% confidence intervals.

[a] Luminosity values were calculated assuming a distance of 9 Mpc to He 2–10.

[b] Parameters in the *Chandra* fits for the nuclear and diffuse components are determined from the fit to the nuclear and extended source regions, respectively, as described in Section 2.1.

[c] The spectra for the two *XMM* observations are fitted simultaneously, with parameters for the diffuse (MEKAL) component tied between the two observations, as described in Section 2.2.

components, and local absorption for the VMEKAL component ($N_{\mathrm{H,Diffuse}} = 9.7 \times 10^{20}$ cm^{-2}). The absorption on the power-law component ($N_{\mathrm{H,Nuclear}}$) was allowed to float. Absorption is computed using the tbabs model (Wilms et al. 2000). In XSPEC notation, the source model is given by:

$$\texttt{Source} = \mathrm{tbabs_{Gal}}\left(\mathrm{tbabs_{Diffuse}} * \mathrm{VMEKAL} + \mathrm{tbabs_{Nuclear}} * \mathrm{powerlaw}\right). \quad (1)$$

We first fit this model to the spectrum from the nuclear (2.″25 radius) source region, to obtain the strongest possible constraint on the emission from the unresolved hard component. With relatively few counts at high energies we obtain poor constraints on the hard-X-ray photon index, so this is fixed to the canonical AGN value of $\Gamma = 1.8$. (Repeating the fit for values of intrinsic Γ varying within a range typical for AGN, $1.4 < \Gamma < 2.2$ Tozzi et al. 2006, produces no significant change in the unabsorbed flux.) The fit yields $N_{\mathrm{H}} = (4.61^{+1.67}_{-1.26}) \times 10^{22}$ cm^{-2}, indicating substantial absorption. We next fit the same model to the spectrum from the extended source region (a circle centered on the nuclear region with 16.″8 radius), but fix the N_{H} value on the power-law component to that obtained for the nuclear spectrum. We obtain a consistent and nearly identical flux for the hard power-law component between the extended and nuclear regions, but a substantially brighter diffuse (VMEKAL) component in the extended region, with best-fit $k_T = 0.65 \pm 0.03$ keV. This confirms that for an even larger extraction region such as those used for *XMM* and *ASCA*, the hard spectral component can be associated with the compact nuclear source. The best-fit fluxes and spectral parameters are given in Table 2. We quote intrinsic (unabsorbed) fluxes and luminosities for the hard nuclear component, and observed (absorbed) fluxes for the soft diffuse component. For direct comparison with the *XMM* analysis, we have also extracted a *Chandra* spectrum with somewhat larger radius of 36″, corresponding to the *XMM* source region described in the next section (Figure 1). Using this larger source region has no significant effect on the spectral parameters.

2.2. XMM-Newton

We use two subsequent observations of He 2–10 by *XMM* to constrain the long-term variability of the source. The *XMM* observations on 2004 May 27 and 2011 May 11 have exposure times of 42 and 27 ks, respectively. For both *XMM* observations, we reduced, cleaned, and extracted spectra from all three CCD cameras: pn, MOS1, and MOS2. After spectral extraction and analysis, the MOS1 and MOS2 data yielded significantly lower S/N at energies >2 keV compared to the pn detector, so that no useful constraints were obtained on the hard emission from the nuclear point source. In what follows we therefore focus on results from the pn.

The source extraction regions were 36″ in radius, chosen to provide a balance between extracting as many counts as possible from the source and minimizing the background. (As a check, we have repeated the analysis using a smaller source region of 25″ radius, and obtain essentially identical results with marginally larger uncertainties.) The *Chandra* images (Figure 1) show that the extent of both the nuclear and diffuse components are substantially smaller than the 36″ extraction region, such that they can both be considered as approximate point sources for the *XMM* analysis. In both data sets the source region was on-axis and did not lie on any chip gaps. We extracted pn spectra for counts in the energy range 0.2–15 keV and with event patterns 0–4. Response files were produced from the *XMM-Newton* Current Calibration Files corresponding to the time of this observation. The source ARF is calculated including a correction for photons falling outside the extraction region. This energy-encircled fraction (EEF) varies with energy but is ≈85% at 5 keV. The source spectrum is described with the same model as for *Chandra*, consisting of VMEKAL and power-law components (Equation (1)).

To maximize the number of counts in the background spectra and thus achieve the highest possible S/N, we extracted the background spectrum from a large annulus of outer radius 3 arcmin around the source. Based on a number of trials, the 3 arcmin annulus was determined to provide the optimum number of background counts without needing to account for the variation in background flux at larger off-axis angles. Using the SAS command `edetect_chain`, five sources in the pn field of view were detected and subsequently excluded from the

background region. With these sources excluded, the background region is ≈23 arcmin^2 in area, or 20 times larger than the source region. Because the background emission is extended in nature, the ARF for the background region did not include an EEF correction.

The pn background spectrum was fitted with two components. The instrumental background is modeled by a power-law continuum, plus Gaussian emission lines caused by fluorescence (Al K-α at 1.5 keV and CuNi K-α at 8.5 keV (Carter & Read 2007). Because this instrumental background is produced internally to the detector and is not affected by the mirror response, in modeling the observed counts it was was convolved with an RMF but not multiplied by an ARF. The background line energies were determined from fitting each line individually, and then fixed for the full spectral analysis, while the intrinsic line widths are fixed to be consistent with zero.

The sky background component is dominated by the diffuse soft cosmic X-ray background (CXB), which can be modeled as thin-thermal emission (Hickox & Markevitch 2006, 2007). We used an APEC model for this component, to match the spectral shape obtained by Hickox & Markevitch (2006) in fitting the unresolved CXB spectrum in the *Chandra* Deep Fields, fixing $kT = 0.17$ keV and allowing the normalization to float. The hard (>2 keV) CXB can be described as a power law owing to the summed emission from a large number of AGN (e.g., Hickox & Markevitch 2006). We did not include this as a separate component here, as the average expected numbers of counts is <2% of the instrumental background, so its small contribution to the total background flux can be effectively accounted for in our modeling of the instrumental background.

The full model for the total observed emission in the *XMM* source region is:

$$\texttt{Data} = \texttt{Source} + \texttt{Instrumental BG} + \texttt{Sky BG}. \quad (2)$$

The source spectrum is modeled by an absorbed VMEKAL and power law (Equation (1)), while the background components are modeled, in XSPEC notation, as:

$$\texttt{Instrumental BG} = \text{powerlaw} + \text{gauss} + \text{gauss} + \text{gauss} \quad (3)$$

and

$$\texttt{Sky BG} = \text{APEC}, \quad (4)$$

where `Instrumental BG` is convolved with the RMF only, while `Source` and `Sky BG` are convolved by the RMF and multiplied by the ARF.

As discussed below, the fluxes of the nuclear power-law component in the *XMM* observations are significantly smaller than that observed for *Chandra*. To most accurately extract the weak hard-X-ray signal from the significant background, we modeled the data by simultaneously fitting the source and background spectra, using the model given in Equation (2). We account for the differences in area between the source and background regions by setting the `AREASCAL` parameter on the background spectrum. The spectral parameters of the instrumental and sky backgrounds were fixed to be equal for the source and background spectra. The source component is also included in the background spectrum, but multiplied by a factor 5×10^{-3} to approximately model the flux scattered outside the source region into the background region. (The scaling factor accounts for both the energy encircled fraction and the relative area of the source and background regions; the ultimate fit parameters are insensitive to the precise value of this factor.)

Because the soft (VMEKAL) emission from the source is diffuse (with a diameter of ≈5″ or 200 pc), and thus a light-crossing time much longer than the separation in time between observations, it should not be observed to vary in our data. Therefore, to maximize the statistical power of our modeling, we fitted the 2004 and 2011 *XMM* spectra simultaneously, tying the temperatures and normalizations of the VMEKAL and APEC components between the two data sets. We allowed the the nuclear power-law normalization to float, along with the instrumental background parameters (the particle background in the detectors should not be perfectly constant for the duration of the mission). We thus performed a simultaneous fit to four spectra: source and background spectra from each of the 2004 and 2011.

The results of the spectral fitting are shown in Figure 2 and listed in Table 2. We observe a clear decrease in the flux of the hard nuclear component between the 2001 *Chandra* and 2004 *XMM* observations. This is demonstrated in Figure 3, in which we show the 2004 *XMM* pn spectrum fitted with the 2001 *Chandra* best-fit model, with no model for the *XMM* background included. This shows that the hard source flux has dropped dramatically from the *Chandra* level, even before accounting for the *XMM* background. We observe a further, less significant decrease between the 2004 and 2011 *XMM* observations, while the flux of the diffuse (VMEKAL) component is consistent with no variation from the *Chandra* observation. We also observe evidence for a decrease in absorption on the nuclear component, with $N_{\rm H,Nuclear}$ consistent with zero. The best-fit *kT* of the VMEKAL component for *XMM* is close but not fully statistically consistent with the *Chandra* data ($0.58^{+0.02}_{-0.03}$ keV compared to 0.65 ± 0.03 keV). Fixing this temperature to the *Chandra* value has a negligible effect on the flux of the diffuse component, but decreases the flux of the hard nuclear component by ≈15%. This results in an even larger observed drop in flux compared to the *Chandra* data; in the following discussion we will conservatively consider the smaller change in flux obtained when the VMEKAL *kT* allowed to float for *XMM*. The flux of the APEC component, representing the soft diffuse CXB, corresponds to a 0.5–2 keV surface brightness of $(2.9 \pm 0.5) \times 10^{-12}$ erg cm^{-2} s^{-1} deg^{-2}, similar to the soft background intensity obtained in the *Chandra* Deep Fields (Hickox & Markevitch 2006). The overall implications of the spectral fitting results are discussed in Section 3.

One potential uncertainty in our spectral analysis arises from the implicit assumption that the instrumental and sky background in the source region has the same surface brightness to the emission in the background region. It is possible that fluctuations in the background could cause this assumption to be invalid, leading to over- or under-subtraction of the background, particularly at energies >2 keV where the background dominates the signal. To directly check the level of possible fluctations, we extracted the 2–10 keV counts in 80 circular regions of 36″ radius (equal to the source region) surrounding the source region. We avoid chip gaps and obvious bright sources, noting that there is no bright point source detected within 36″ in the 2–8 keV *Chandra* image (Figure 1). The 2–10 keV counts in these apertures are approximately normally distributed, with mean (dispersion) of 239 (19) and

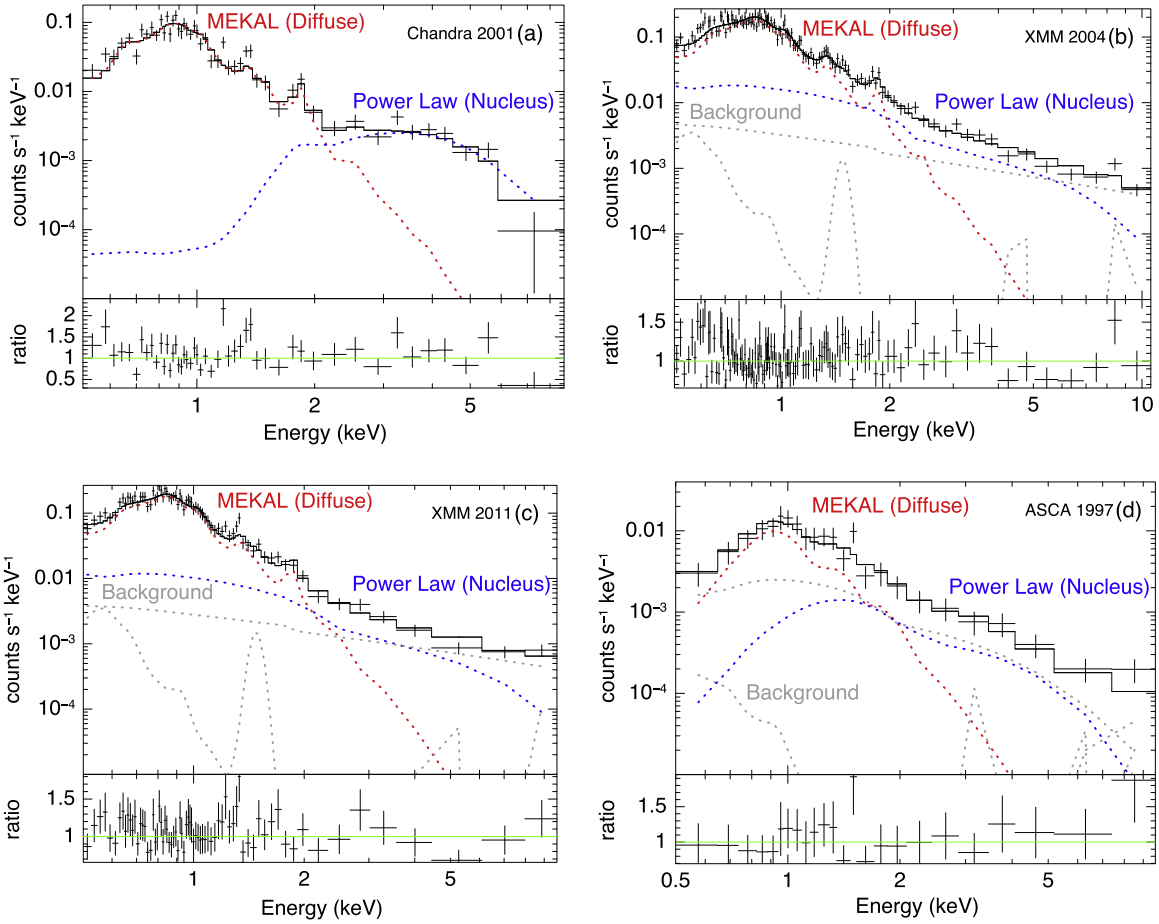

Figure 2. X-ray spectra including model fits and residuals, for four X-ray observations of He 2–10. Each component of the model fitted to the data are shown as dotted lines: the diffuse VMEKAL component (red) and nuclear power law (blue). For the *Chandra* observation (a) the background was subtracted before spectral fitting, while for the *XMM* (b), (c) and *ASCA* (d) observations, the background spectra are fitted by a model(shown by the gray lines) simultaneously with fitting of the observed source spectrum. There is a strong and significant detection of the hard nuclear power-law component in the 2001 *Chandra* (a) observation (clearly visible as a point source in Figure 1). The hard component is significantly weaker in the *XMM* observations (b), (c) indicating variability by approximately an order of magnitude. The hard component is also detected, at lower significance, in the 1997 *ASCA* spectrum (d).

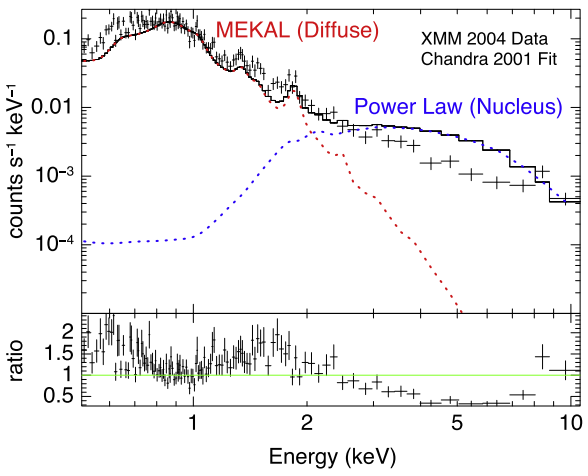

Figure 3. Spectrum of the 2004 *XMM* observation, fitted with the source spectrum from the 2001 *Chandra* observation. This fit includes no subtraction or modeling of the *XMM* background. This large excess of the model over the data at high energies clearly illustrates the dramatic decrease in the flux of the hard nuclear component between 2001 and 2004, independent of the methods used to account for the *XMM* background.

138 (15) counts for 2004 and 2011, respectively. We conclude that our modeling of the background in the source region is dominated by statistical error rather than any systematic uncertainty due to background fluctuations.

2.3. *ASCA*

As a measurement of the baseline level of flux prior to the *Chandra* observations, we also utilize observations of He 2–10 from *ASCA* in 1997. Due to *ASCA*'s poor angular resolution and sensitivity relative to *Chandra* and *XMM*, it provides relatively weak constraints on the source flux, particularly in the hard nuclear component. We will therefore focus our conclusions primarily on the *Chandra* and *XMM* data, but will utilize the *ASCA* data here as a useful check on our conclusions.

He 2–10 was observed by *ASCA* for a total of 39.8 ks on 1997 November 30. We used Xselect v2.4b to remove time intervals of high background for a net exposure of 22.4 ks, and to extract source and background spectra from the cleaned event files. We extracted a spectrum in the energy range between 0.5–10.5 keV, using a source extraction region of 1.45 arcmin in radius. This source region was chosen to contain

as much of the source flux as possible (the energy encircled fraction is 50%) while minimizing the contribution from background. We extracted a background spectrum from a rectangular annulus of area ≈5 times that of the source region, located around the source position but excluding the source region. The RMF and ARF response files were generated for each chip using the commands `sisrmg` and `ascaarf`, respectively. Furthermore, the spectra from the two chips SIS0 and SIS1 were added using the HEASOFT command `mathpha`, while the response files were added with area dependent weights using the commands `addarf` and `addrmf`. As discussed in Section 2.2, the source ARF includes a correction for the energy encircled fraction, while the background ARF does not.

As with *XMM*, we modeled the *ASCA* data by fitting the source and background spectra simultaneously, modeling the scattered flux in the background region assuming an energy-encircled fraction of 0.5. The instrumental background was modeled with a power law plus five Gaussian emission lines; three were included in the model as narrow fluorescence lines stemming from the device itself at 6.5, 7.5, and 8.2 keV, which are the Fe and Ni K-α lines and the Ni K-β line.[9] Another Gaussian at 3.3 keV of unknown origin was introduced to fit a feature of the background spectrum, while the final Gaussian was a broad line at 11 keV that modeled the internal background above 7 keV to account for the steepness of the power law.

We utilized the same source and sky background models as for *XMM* (Equations (1) and (4)). Because they cannot be well-constrained owing to the poor photon statistics, the surface brightness of the APEC component and the VMEKAL temperature are fixed to the values obtained with *XMM*, and the photon index of the power law is again fixed to $\Gamma = 1.8$. (Allowing the VMEKAL temperature to float yields a significantly higher $kT \approx 0.9$, inconsistent with the *XMM* and *Chandra* results, but has a negligible effect on the total fluxes of the diffuse and nuclear components.) The results of the *ASCA* spectral fitting are shown in Figure 2 and listed in Table 2. We obtain a significant detection of both the diffuse and nuclear spectral components, although with significantly larger uncertainties than in the *Chandra* and *XMM* data. In contrast to the *XMM* observations, the fit yields significant nuclear absorption consistent with the *Chandra* value, although the precise value of $N_{\rm H}$ is poorly constrained.

3. RESULTS AND DISCUSSION

The long-term X-ray light curve of He 2–10, showing variations in the VMEKAL and power-law components, are shown in Figure 4. The diffuse component shows no significant variability over the four observations, as expected for emission from a large-scale diffuse plasma. In contrast, it is immediately clear that there is significant variability in the hard power-law component. The luminosity of the nuclear source decreased significantly between the 2001 *Chandra* and 2004 *XMM* observations, and by approximately an order of magnitude between 2001 and the 2011 *XMM* observation. (We note that our overall conclusions are unchanged if we use observed hard fluxes, which differ by roughly 30% from the values shown in the Table 2 for the *Chandra* and *ASCA* observation and remain constant for *XMM* due to the decreased levels of obscuration.)

[9] https://heasarc.gsfc.nasa.gov/docs/asca/newsletters/sis_back2.html

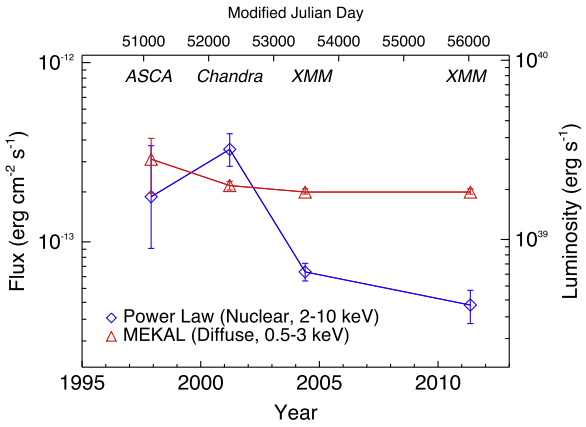

Figure 4. Fourteen year light curve of He 2–10 with 90% confidence errors shown. The hard nuclear flux (blue) declines between the 2001 *Chandra* and 2011 *XMM* observations by nearly an order of magnitude. In contrast, the soft diffuse flux (red), remains approximately constant between the four observations.

The variation in the light curve of hard spectral component He 2–10 over approximately an order of magnitude in L_X confirms that this emission is the result of a single object, rather than several separate sources. This allows us to perform comparisons to other individual astrophysical sources. One class of object that can have similar X-ray and luminosities and amplitudes of variability is SNe (see Dwarkadas & Gruszko 2012 for a compilation of published SN X-ray light curves). However, an SN interpretation for the nuclear source is inconsistent with the radio properties. The radio flux of He 2–10 has been measured at 5 GHz with the VLA in 1994 (0.89 ± 0.18 mJy; Kobulnicky & Johnson 1999) and 2004 (0.86 ± 0.02 mJy; Reines et al. 2011), implying no significant change in the radio flux with time. Long Baseline Array measurements in 2011 at 1.4 GHz yield a flux of 0.98 ± 0.21 mJy in a compact source on ≈1 pc spatial scales; assuming a typical radio spectral index, this implies that roughly half of the observed 5 GHz flux comes from the central compact source (Reines & Deller 2012). High Sensitivity Array observations in 2005 did not detect the compact source on extremely small (∼0.1 pc) spatial scales (Ulvestad et al. 2007), placing a lower limit on its spatial extent. This rules out the presence of a single very young SN, however, the total radio luminosity of the source would imply that any single SN must be at most decades old (Fenech et al. 2010).

With these constraints in mind, we test whether the nuclear source in He 2–10 is consistent with a (relatively) evolved SN explosion, by comparing its (unabsorbed) soft-X-ray and 5 GHz radio light curves to a sample of seven SNe that have both radio and X-ray measurements in the compilations of Dwarkadas & Gruszko (2012) and Weiler et al. (2002). Assuming that the nuclear source in He 2–10 has a relatively constant 5 GHz flux between 1994 and 2004, and conservatively assigning all of the 5 GHz flux observed with the VLA (≈0.9 mJy) to the central compact component, we find that the ratio of X-ray (0.5–2 keV) to radio (νF_ν at 5 GHz) for He 2–10 is $\sim 5 \times 10^3$. This is more than an order of magnitude larger than the typical X-ray to radio flux ratio for X-ray-detected SNe at ages >1 year, and 2.5 times larger than the most extreme observed values, in SNe 1980K and 1970G. Furthermore, the detection of the nuclear hard-X-ray component in the *ASCA* observation indicates that the X-ray light curve rises or

remains constant, and then declines sharply over a few years. This behavior is unusual for SNe; of the eight SN X-ray light curves in the compilation of Dwarkadas & Gruszko (2012) that extend beyond 10 years, none shows a similar sudden, rapid decline on these timescales. We also note that the X-ray to radio flux ratio is consistently at least two to three orders of magnitude *smaller* than the typical ratio of X-ray to compact radio flux for ULXs, for which the compact sources tend to be weak or undetected in the radio (e.g., Middleton et al. 2013; Wolter et al. 2014). Given the observed X-ray light curve and the ratio of X-ray and radio luminosities, we conclude that the observations do not favor an SN or ULX origin for the nuclear source.

In contrast, the significant variability of the hard nuclear X-ray source in He 2–10 is consistent with its identification as an accreting massive BH, in comparison to the X-ray variability of known low-mass AGN. The Sdm spiral galaxy NGC 4395, at a distance of only 4 Mpc, contains a BH of mass $3.6 \times 10^5\,M_\odot$, whose hard component, as is shown in King et al. (2013), can vary by a factor of five on a timescale of just one day. The nearby edge-on Seyfert 2 galaxy NGC 4945, with a BH mass obtained through observations of its H_20 megamaser of $\approx 10^6\,M_\odot$, shows intrinsic variability (measured at >8 keV by *RXTE* and *Swift*/BAT) of at least an order of magnitude on timescales of days to weeks (e.g., Mueller et al. 2004; Marinucci et al. 2012). The AGN in the nearby Seyfert 1 galaxy NGC 4051 ($M_{\rm BH} = 1.73 \times 10^6\,M_\odot$; Denney et al. 2009) has been observed to vary in X-ray luminosity by more than an order of magnitude over ∼year timescales (Uttley et al. 1999). This limited survey confirms that X-ray variability over a large dynamic range on timescales of years is not uncommon among relatively low-mass AGNs. Therefore, the decreased observed luminosity after the *Chandra* observations could either be due to short timescale fluctuations occurring precisely at the time of the observation, as in NGC 4945, or part of a general trend of long timescale variability, similar to objects like NGC 4051.

Support for A.E.R. was provided by NASA through the Einstein Fellowship Program, grant PF1-120086, and the Hubble Fellowship Program. R.C.H. acknowledges support from the Dartmouth College Class of 1962 Faculty Fellowship. G.R.S. acknowledges support from an NSERC Discovery Grant. This research has made use of data, software and/or web tools obtained from NASA's High Energy Astrophysics Science Archive Research Center (HEASARC), a service of Goddard Space Flight Center and the Smithsonian Astrophysical Observatory.

REFERENCES

Allen, D. A., Wright, A. E., & Goss, W. M. 1976, MNRAS, 177, 91
Arnaud, K. A. 1996, in ASP Conf. Ser. 101, Astronomical Data Analysis Software and Systems V, ed. G. H. Jacoby, & J. Barnes (San Francisco, CA: ASP), 17
Carter, J. A., & Read, A. M. 2007, A&A, 464, 1155
Denney, K. D., Watson, L. C., Peterson, B. M., et al. 2009, ApJ, 702, 1353
Dewangan, G. C., Mathur, S., Griffiths, R. E., & Rao, A. R. 2008, ApJ, 689, 762
Dwarkadas, V. V., & Gruszko, J. 2012, MNRAS, 419, 1515
Fenech, D., Beswick, R., Muxlow, T. W. B., Pedlar, A., & Argo, M. K. 2010, MNRAS, 408, 607
Hickox, R. C., & Markevitch, M. 2006, ApJ, 645, 95
Hickox, R. C., & Markevitch, M. 2007, ApJL, 661, L117
Johnson, J. L., & Bromm, V. 2007, MNRAS, 374, 1557
Johnson, K. E., & Kobulnicky, H. A. 2003, ApJ, 597, 923
King, A. K., Miller, J. M., Reynolds, M. T., et al. 2013, ApJL, 774, L25
Kobulnicky, H. A., & Johnson, K. E. 1999, ApJ, 527, 154
Kobulnicky, H. A., & Martin, C. L. 2010, ApJ, 718, 724
Lemons, S., Reines, A., Plotkin, R., Gallo, E., & Greene, J. 2015, ApJ, in press (arXiv:1502.06958)
Liedahl, D. A., Osterheld, A. L., & Goldstein, W. H. 1995, ApJL, 438, L115
Marinucci, A., Risaliti, G., Wang, J., et al. 2012, MNRAS, 423, L6
Merloni, A., Heinz, S., & di Matteo, T. 2003, MNRAS, 345, 1057
Mewe, R., Gronenschild, E. H. B. M., & van den Oord, G. H. J. 1985, A&AS, 62, 197
Middleton, M. J., Miller-Jones, J. C. A., Markoff, S., et al. 2013, Natur, 493, 187
Mueller, M., Madejski, G., Done, C., & Zycki, P. 2004, in AIP Conf. Ser. 714, X-ray Timing 2003: Rossi and Beyond, ed. P. Kaaret, F. K. Lamb, & J. H. Swank (Melville, NY: AIP), 190
Reines, A. E., & Deller, A. T. 2012, ApJL, 750, L24
Reines, A. E., Greene, J. E., & Geha, M. 2013, ApJ, 775, 116
Reines, A. E., Plotkin, R. M., Russell, T. D., et al. 2014, ApJL, 787, L30
Reines, A. E., Sivakoff, G. R., Johnson, K. E., & Brogan, C. L. 2011, Natur, 470, 66
Roberts, T. P. 2007, Ap&SS, 311, 203
Secrest, N. J., Satyapal, S., Gliozzi, M., et al. 2015, ApJ, 798, 38
Smith, R. K., Brickhouse, N. S., Liedahl, D. A., & Raymond, J. C. 2001, ApJL, 556, L91
Tozzi, P., Gilli, R., Mainieri, V., et al. 2006, A&A, 451, 457
Ulvestad, J. S., Johnson, K. E., & Neff, S. G. 2007, AJ, 133, 1868
Uttley, P., McHardy, I. M., Papadakis, I. E., Guainazzi, M., & Fruscione, A. 1999, MNRAS, 307, L6
Volonteri, M. 2010, A&ARv, 18, 279
Weiler, K. W., Panagia, N., Montes, M. J., & Sramek, R. A. 2002, ARA&A, 40, 387
Wilms, J., Allen, A., & McCray, R. 2000, ApJ, 542, 914
Wolter, A., Rushton, A. P., Mezcua, M., et al. 2014, PoS, in press (arXiv:1412.5643)